A Tool for Alignment and Averaging of Sparse Fluorescence Signals in Rod-Shaped Bacteria

Goudsmits, Joris M. H.; van Oijen, Antoine M.; Robinson, Andrew

Published in:
Biophysical Journal

DOI:
10.1016/j.bpj.2016.02.039

Publication date:
2016

Biophysical *Journal*
Computational Tool

Biophysical Society

A Tool for Alignment and Averaging of Sparse Fluorescence Signals in Rod-Shaped Bacteria

Joris M. H. Goudsmits,[1] Antoine M. van Oijen,[1,2] and Andrew Robinson[1,2,*]
[1]Zernike Institute for Advanced Materials, University of Groningen, Groningen, the Netherlands; and [2]School of Chemistry, University of Wollongong, Wollongong, New South Wales, Australia

ABSTRACT Fluorescence microscopy studies have shown that many proteins localize to highly specific subregions within bacterial cells. Analyzing the spatial distribution of low-abundance proteins within cells is highly challenging because information obtained from multiple cells needs to be combined to provide well-defined maps of protein locations. We present (to our knowledge) a novel tool for fast, automated, and user-impartial analysis of fluorescent protein distribution across the short axis of rod-shaped bacteria. To demonstrate the strength of our approach in extracting spatial distributions and visualizing dynamic intracellular processes, we analyzed sparse fluorescence signals from single-molecule time-lapse images of individual *Escherichia coli* cells. In principle, our tool can be used to provide information on the distribution of signal intensity across the short axis of any rod-shaped object.

INTRODUCTION

In eukaryotic cells, many cellular processes are physically separated from each other within organelles. Bacterial cells do not typically display such compartmentalization, yet fluorescence microscopy studies have revealed that many bacterial proteins localize to distinct subregions within cells (1). Bacterial cells usually consist of a cell wall (composed of one or two membrane bilayers, peptidoglycan and lipopolysaccharide) and the aqueous material it surrounds, known as the cytosol (2). The chromosomal DNA, referred to as the nucleoid, resides within the center of the cytosol (1). When fluorescently tagged and imaged, cytosolic proteins produce diffuse signal throughout the cell as a result of diffusion at a timescale faster than the frame duration (Fig. 1 *A*). Particularly large proteins are excluded from the nucleoid mass and observed to concentrate in the periphery of the cytosol (1). Proteins that associate with membranes, or that reside in the area between two membranes (the periplasm), are confined to the cell edge. In conventional microscopy images that present fluorescence signal from a large number of molecules, these latter proteins typically present as rings that trace the outline of the cell (Fig. 1 *A*). Bacteria also contain structural proteins that have a variety of different localization patterns. FtsZ, for example, forms a distinctive ringlike structure at the midcell before cell division (3,4).

Ordinarily, proteins studied by fluorescence microscopy are expressed at relatively high levels within cells (1). In this case, proteins distribute homogenously throughout a particular subcellular region and thus the localization behavior of a protein is usually immediately obvious from inspection of microscope images (Fig. 1 *A*). Some proteins, however, produce patchy distributions with few features present in each cell. This is particularly true of low-abundance proteins, which can be imaged using single-molecule fluorescence microscopes (1). In this case, there are too few labeled molecules in each cell to uniformly stain the subcellular region to which the protein is localized (Fig. 1 *B*). As a result, the localization behavior of the protein of interest cannot be determined by direct inspection of images.

To determine the cellular locations of proteins that produce patchy distributions, it is necessary to combine information from many cells. The most common approach is to use cell segmentation packages, such as MicrobeTracker (5), CellProfiler (6,7), Schnitzcells (8), PSICIC (9), BactImAS (10), and Oufti (11). The programs measure fluorescence signals across many cells by first assigning outlines for each individual cell based on bright field images, then determining the positions of features within the cells using the fluorescence images, and finally mapping the relative locations of features along the long and short axes of the cell. Cell segmentation is a powerful means to extract highly

Submitted October 8, 2015, and accepted for publication February 16, 2016.

*Correspondence: andrewr@uow.edu.au

Editor: Rong Li.
http://dx.doi.org/10.1016/j.bpj.2016.02.039

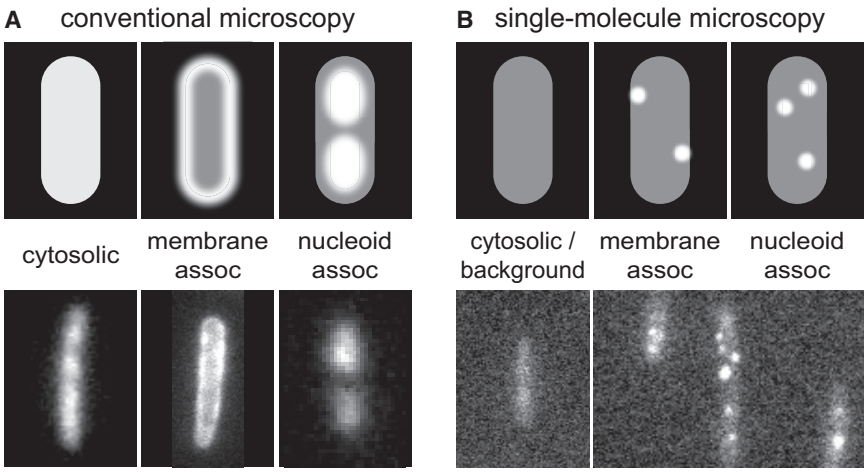

FIGURE 1 Localization patterns of fluorescent proteins in bacterial cells. (*A*) Common localization patterns observed using conventional wide-field fluorescence microscopy. (*Top row*) Schematic representations of cells in which a cytosolic protein, a membrane-associated protein, and a nucleoid-associated protein have been fluorescently labeled. (*Bottom row*) Example microscope images for each localization type (cytosolic YPet; membrane-associated LacY-eYFP. Nucleoid-associated SYTOX orange stain; Thermo Fisher Scientific, Rochester, NY). (*B*) Equivalent patterns observed with single-molecule fluorescence microscopy. (*Top row*) Schematic examples of localization patterns for low-abundance proteins. (*Bottom row*) Example images of a low-abundance fluorescent protein (UmuC-mKate2) expressed in *E. coli* cells. The cell in the left image contains no foci. The right image shows cells with multiple foci, localized to either the membrane or the cytoplasm. Due to the low density of labeled molecules, a generalized localization behavior cannot be resolved from inspection of the image alone. Analyzing the position of all single spots in a series of images would allow the localization to be generalized.

detailed information on fluorescence signals across cell populations (12), many even operating with subpixel resolution (5,9,11). Once the parameters are trained, many algorithms are highly automated, allowing single-cell level analysis on large datasets, including time-lapse series (13–15). Many of the limitations of early packages, such as difficulties working with non-rod-shaped cells or fluorescently labeled structures other than punctate foci, have been overcome in the recently released package Oufti (11).

Cell segmentation techniques do have some disadvantages, however. While they are generally designed to be flexible, working with different cell types and images, they are usually built with a specific set of measurements in mind. Because of differences in cell size and morphology as well as differences in microscope objectives, light sources, and cameras, the algorithms typically require extensive tuning of parameters, often achieved through training protocols. In some cases—for instance, where images contain some cells that are partially or completely out-of-focus or when cells change shape during the course of a time-lapse measurement—cell segmentation may not work well at all. While some cell segmentation programs have been available for several years and are widely used (5,11), many researchers still prefer to write their own cell segmentation software to fulfill particular needs that are not met by existing packages (15–18). Another drawback of cell segmentation approaches is that they require either high-resolution, high-contrast images (typically, phase-contrast, bright field images) or the fluorescent labeling of cells (12), which may not be accessible to all researchers. Beyond these points, assignment of cell outlines is computationally expensive and, in certain situations, manual intervention is required to remove poorly fit outlines.

Here we present a tool that complements cell segmentation approaches, rapidly extracting the average location of fluorescence signals from images containing large numbers of rod-shaped bacterial cells. While our approach does not extract the same level of information detail as cell segmentation, it requires very little parameterization and operates in a highly automated and relatively unbiased manner. The method requires relative low cell density, i.e., cells should be separated by at least the space equal to one cell-width. Our tool creates subsections of images, identifies those that contain cells, and aligns the cells along the vertical axis using structure tensors and Fourier transforms. Fluorescence signals from aligned cells can then be overlaid to examine the distribution of fluorescent proteins along the short axis of the cell. Our highly automated technique works with raw microscopy images and circumvents the need for assigning cell outlines. Our tool is not restricted to analysis of punctate foci; it can be used to generalize the localization of any type of fluorescent feature. In addition to producing overlays, our tool can apply autocorrelation to sensitively identify repeating patterns within the aligned cells, such as those produced by membrane-associated proteins. Our tool is primarily intended for use with time-lapse data, allowing time-dependent changes in protein localization to be monitored. It is further possible to postsynchronize images based on fluorescence intensity to visualize dynamic processes where changes in protein levels correlate with change in protein localization. Using data from known cytosolic and membrane-bound proteins to calibrate intensities across averaged cross sections, we show that it is further possible to quantify relative amounts of protein present in the cytosol or bound to membrane.

MATERIALS AND METHODS

The cell alignment algorithm is implemented in MATLAB (The MathWorks, Natick, MA). The relevant scripts can be found in Data S1. Image preparation steps are performed using the open-source image processing software ImageJ (The National Institutes of Health, Bethesda, MD (19)).

Data collection

We reanalyzed images previously recorded on a wide-field single-molecule fluorescence microscope (20). Briefly, to collect fluorescence images with single-molecule sensitivity, high-power laser excitation was coupled into an inverted fluorescence microscope body (IX-81; Olympus, Melville, NY) equipped with a 1.49 NA 100× objective and a 512 × 512 pixel EM-charge-coupled device camera (C9100-13; Hamamatsu, Hamamatsu City, Japan). Cells were imaged within flow cells that were built upon glass coverslips derivatized with APTES (3-aminopropyl triethoxy silane; Sigma-Aldrich, St. Louis, MO). We reanalyzed data from *Escherichia coli* strains EAW191 (*umuC-mKate2*, containing the plasmid pBAD-LacY-eYFP) and EAW282 (*dnaX-YPet, umuC-mKate2*). Further details on image acquisition, sample preparation, and bacterial strains used can be found in Robinson et al. (20).

Image preparation

The cell-alignment algorithm identifies cells within bright field images. To enhance the contrast of cells within these images we preprocessed them in ImageJ (19). Cell-containing bright field images were first background-corrected by dividing each image by an image of an empty field to enhance the contrast of the cells against the background. To further enhance contrast, a rolling-ball background subtraction (ImageJ: Subtract Background) was then applied, using a rolling-ball radius of 15 pixels (with 1 pixel corresponding to 100 nm in object space). Fluorescence images were preprocessed as follows to remove diffuse (low-frequency) fluorescence, a significant proportion of which arose from autofluorescence of the *E. coli* cells: each image was duplicated and a 4-pixel radius median was applied (ImageJ: Filters, Median). This filtered image was subtracted from the original, effectively removing low-frequency signals. As a result, high-frequency features, such as foci and lines around the cell periphery (indicative of nucleoid- or membrane-bound protein), were enhanced. To reduce pixel noise, the frequency-filtered images were further subjected to a 1-pixel radius median filter.

Rotational (orientation) alignment based on structure tensor

Each bright field image was sectioned into square tiles. The dimensions of the tiles are chosen such that most tiles contain either a single cell segment or no cell segment at all. Subsequently, the individual tiles need to be rotated such that the cell segments become oriented in the vertical direction. The correct angle of rotation was obtained using the structure tensor (21,22), which uses intensity-gradient information to determine the orientation of the cell's long axes. The structure tensor is defined as

$$S = \sum_r \begin{bmatrix} (I_x)^2 & I_x I_y \\ I_x I_y & (I_y)^2 \end{bmatrix}, \tag{1}$$

where I_x and I_y are the horizontal and vertical components, respectively, of the gradient at each pixel. The summation index r ranges over all pixels in the image tile. The gradient components I_x and I_y at every pixel are obtained by convolving the corresponding Sobel kernels with the source image A:

$$I_x = \begin{bmatrix} -1 & 0 & +1 \\ -2 & 0 & +2 \\ -1 & 0 & +1 \end{bmatrix} * A, \quad I_y = \begin{bmatrix} -1 & -2 & -1 \\ 0 & 0 & 0 \\ +1 & +2 & +1 \end{bmatrix} * A.$$

The eigenvalues λ_1 and λ_2 (with $\lambda_1 \geq \lambda_2 \geq 0$) and their corresponding orthogonal eigenvectors e_1 and e_2 of S describe the overall gradient features. When $\lambda_1 > \lambda_2$, the image tile has a predominant direction and the eigenvector e_2 is aligned perpendicular to the gradient direction, i.e., along the cell's long edge. When $\lambda_1 \approx \lambda_2$, the image tile is isotropic and does not have a main direction. The degree of anisotropy can be quantified with the coherence C (23),

$$C = \left(\frac{\lambda_1 - \lambda_2}{\lambda_1 + \lambda_2} \right)^2 \tag{2}$$

that ranges from 0 to 1.

Translational (center) alignment based on Fourier transform

Tiles containing vertically oriented cell segments were then projected along the vertical axis to produce line scans of the mean intensity across the short axis of the cell. These line scans were then centered by translating them until the symmetry of the cell-derived signals was maximized (around the line's midpoint). This is achieved by finding the points of real-valued translation r for which the imaginary part of the Fourier transform L_k of the line projection l_n attains its minimum value:

$$\begin{aligned} &\underset{r}{\operatorname{argmin}} \sum_{k=0}^{N-1} |\mathrm{Im}(L_k(r))|, \\ &L_k(r') = L_k \times e^{-2\pi i k r'/N} = \sum_{n=0}^{N-1} l_{n-r'} \times e^{-2\pi i k n/N}, \end{aligned} \tag{3}$$

where N is the total number of samples in l_n. Two solutions exist: one is center-symmetric, the other edge-symmetric. The correct solution is selected based on intensity distribution: in bright field images, cells are typically dark compared to the background.

Line scan analysis

For each valid tile a short-axis cross section (line scan) is created by projecting the fluorescence data along the long axis. Line scans are averaged per data set and normalized to a maximum of 1 for display purposes. The autocorrelation R at lag r' of individual (zero-padded) line scans l_n is calculated as

$$R(r') = \sum_n l_n l_{n-r'}. \tag{4}$$

The value at zero lag, which is mainly determined by noise, is ignored by assigning $R(0) = R(1)$. Then, the autocorrelation is normalized to 1 at zero lag. Autocorrelations are weight-averaged by the integrated intensity of the corresponding line scans and normalized to a maximum of 1 for display purposes.

Postacquisition synchronization

Tiles in time-lapse images were synchronized after acquisition to eliminate temporal heterogeneity in cell responses. Tiles containing time series were synchronized to the time point at which cells reached their maximum fluorescence intensity. First, all slices in the time lapse were blurred with a Gaussian filter of $\sigma \approx 3 \times w_{\mathrm{cell}}$, with w_{cell} the width of the cell. Next, a moving average filter (width, 5 slices) was applied across time points. For each pixel, the time of maximum intensity t_{Imax} is determined. Finally, for every tile the median of t_{Imax} is calculated and used for synchronization.

RESULTS

Principle

A schematic diagram of our workflow is shown in Fig. 2 *A*. Bright field images are used to determine transformation parameters that subsequently allow fluorescence signals of cells to be overlaid. First, a bright field image is sectioned into equally sized square tiles (Fig. 2, *B* and *C*). Their dimensions are typically three to four times the width of the cells. For this study, we used a tile size of 32 × 32 pixels (corresponding to 3.2 × 3.2 μm in object space). With cells being separated at least one time by the cell width, each tile typically contains at most one useful segment from one cell. Smaller tile dimensions would result in increased error in rotational and translational alignment of cell segments; larger tile dimensions would frequently result in tiles containing multiple cell segments. In the next step, tiles are rotationally aligned on the vertical axis of the image using structure tensors (Fig. 2 *D*). Tiles are padded with pixels from neighboring tiles to avoid corner artifacts. The Fourier transform is then used to shift tile images to place cells in the center (Fig. 2 *E*). Tile images are assumed to be periodic in the horizontal direction, meaning that parts shifting out of the tile on one side enter the tile on the opposite side. Finally, tiles that do not meet the following three selection criteria are discarded (Fig. 2 *F*): (1) Empty tiles are rejected based on contrast values, defined as the standard deviation of the pixels. The contrast value used as the selection threshold is determined empirically. (2) Tiles with non-rod-shaped objects are removed by rejecting those with a coherence value (Eq. 2) below a lower limit (typically 0.2; see Supporting Materials and Methods S2.1). (3) Tiles containing incomplete cell cross sections are removed by allowing a maximum translation of $w_{\text{tile}}/2 - w_{\text{cell}}/2$ (which equals 10 pixels or 100 nm in this study), with w_{tile} and w_{cell} being the width of the tile and cell, respectively (see Supporting Materials and Methods S2.2).

The first two selection steps are implemented at the orientation alignment step, significantly reducing computation time for subsequent steps. The entire process is repeated three more times, shifting the positions of tile boundaries (by $w_{\text{tile}}/2$ in the vertical, horizontal, and finally both directions) to prevent cells from being ignored when initially lying on tiles boundaries. Taking into account the cell density and tile size requirements, typically >80% of the cell surface area is analyzed. Some cell segments are analyzed multiple times—especially along the cell's long axis—but this does not affect the end-result, because this is an ensemble method.

The obtained transformations and selection parameters are then applied to the fluorescence images that are corresponding to the bright field images. For each tile, a one-dimensional projection along the vertical axis creates a short-axis cross section (line scan). Finally,

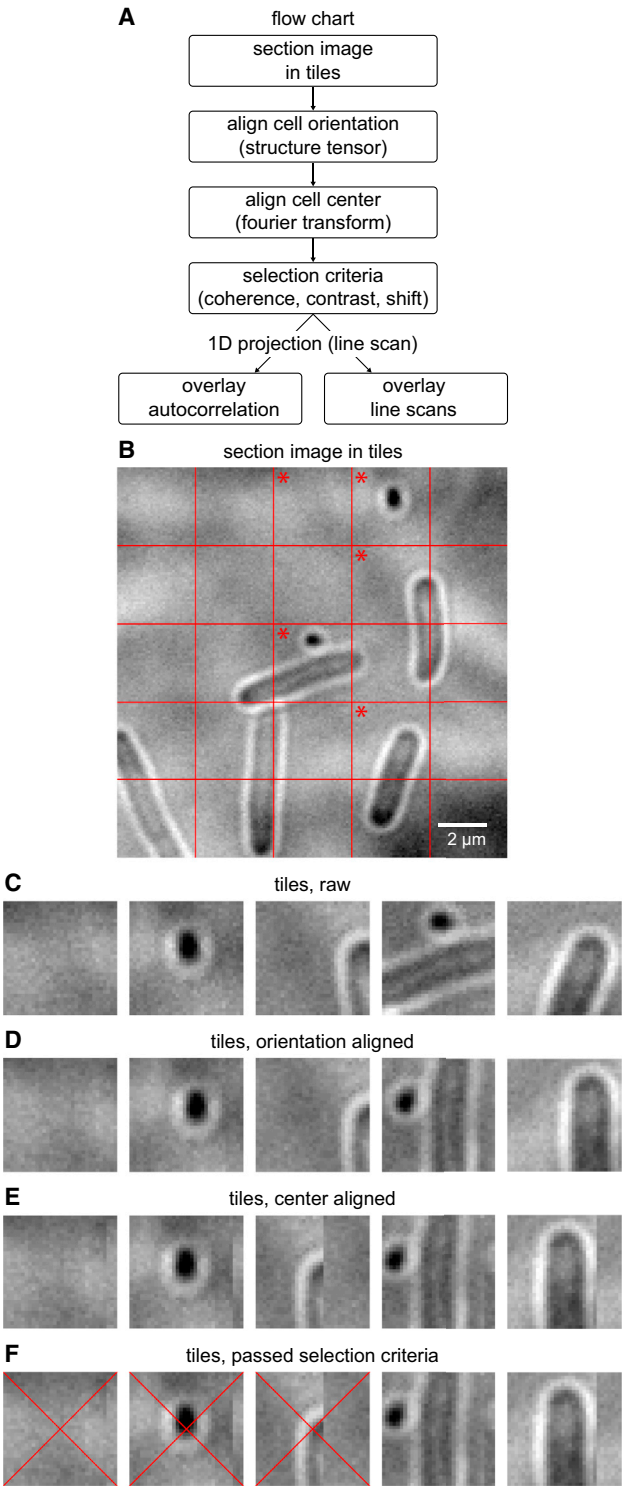

FIGURE 2 Workflow of the algorithm. (*A*) Flow chart summarizing individual processing steps. (*B* and *C*) Bright field images are sectioned in square tiles containing a part of one cell. For illustration of the process, tiles marked with an asterisk are shown in (*C*–*F*). (*D*) Cells are aligned along the vertical axis using structure tensors. (*E*) Tile images are centered with Fourier transformation. (*F*) Tiles that contain nothing (*first image*), non-rod-shaped objects (*second image*), or clipped cells (*third image*) are discarded. One-dimensional projections along the vertical axis (line scans) of the accepted tiles are processed for further analysis. To see this figure in color, go online.

for all identified cells in the population, the line scans and their autocorrelations are overlaid and processed further.

Analysis of fluorescent protein localization within aligned cells

To validate our approach, we analyzed images of *E. coli* cells containing fluorescent fusions of nucleoid- and membrane-associated proteins. The nucleoid-associated protein, DnaX-YPet (a replisome component fused to the YFP variant YPet (20,24)), forms punctate foci on the nucleoid region of the cytosol (Fig. 3 *A*), while the membrane protein, LacY-eYFP (a membrane-integral lactose transporter fused to the YFP variant eYFP (20)), produces a relatively homogeneous signal around the cell periphery (Fig. 3 *B*).

For each protein we analyzed 444 individual images, derived from time-lapse measurements on 12 fields of view. Cells were first aligned using bright field images, following the steps described above. The resulting transformations were applied to the corresponding fluorescence images. Fluorescence along the vertical axis of each tile was compressed to a line scan representing the distribution of signal across the short axis of the cell. These line scans were summed to produce an average line scan for the population as a whole (Fig. 3, *C* and *D*). As expected, cells containing nucleoid-associated DnaX-YPet produce

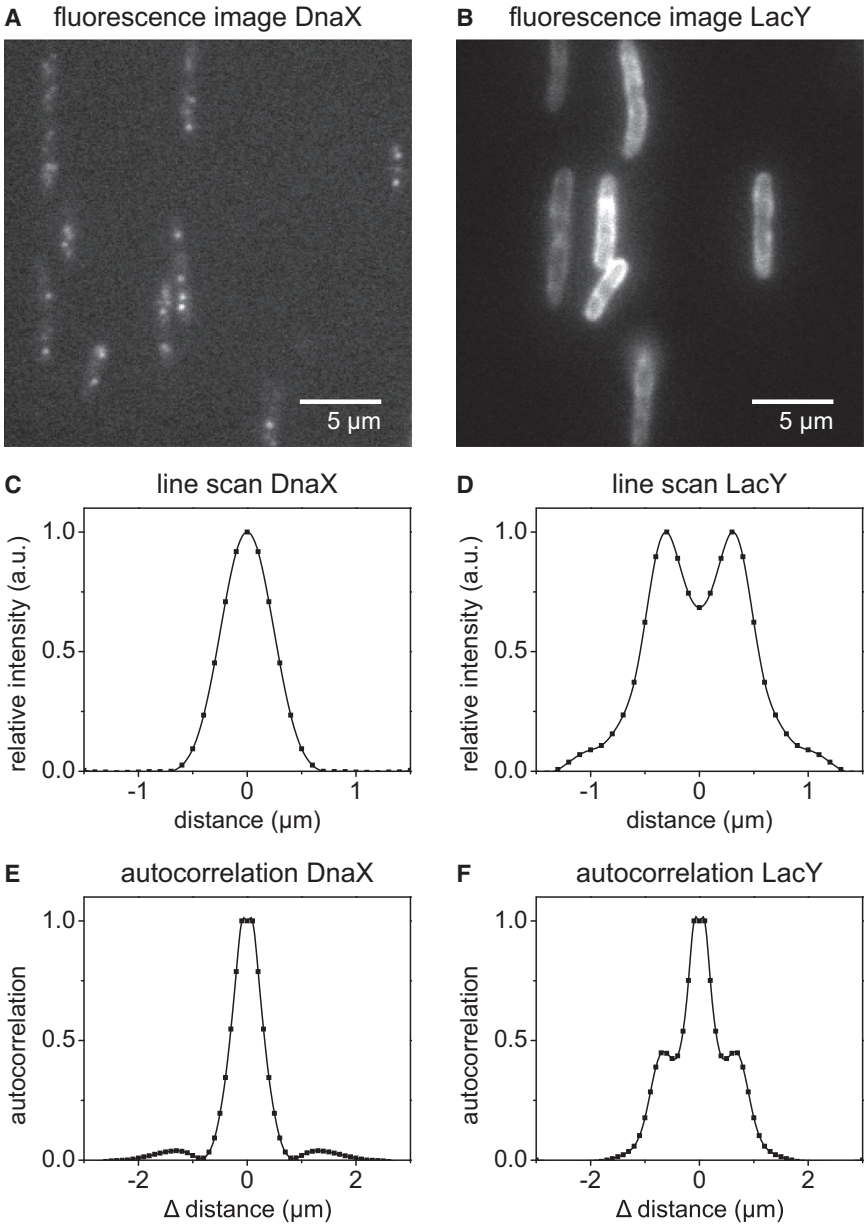

FIGURE 3 Analysis of proteins with known nucleoid-associated (DnaX-YPet) and membrane-associated (LacY_eYFP) distributions. (*A*) Fluorescence image of DnaX-YPet. Punctate foci on the nucleoid region of the cytosol are visible. (*B*) The fluorescent membrane protein LacY-eYFP produces a relatively homogeneous signal around the cell periphery. (*C* and *D*) Average line scans of the entire populations for DnaX and LacY. The cytosolic DnaX shows a single peak; membrane-localized LacY shows two peaks separated by the average cell width. (*E* and *F*) Averaged autocorrelations of the individual line scans for DnaX and LacY. A single broad peak for cytosolic DnaX and strong cross peaks for membrane-bound LacY are observed.

a line scan with a single central peak (Fig. 3 *C*), while cells containing the membrane-localized LacY-eYFP protein produced a line scan with two peaks, separated by ~0.7 μm (the average width of an *E. coli* cell under our conditions; Fig. 3 *D*).

We recently demonstrated the use of autocorrelation to differentiate cytosolic and membrane-associated signals in *E. coli* (20). We found that cytosolic and nucleoid-associated signals produce autocorrelation functions with a single, broad peak, whereas membrane signals produce secondary peaks due to correlations across the two sides of the membrane. In these previous measurements, alignment was achieved to a certain degree by imaging the cells in flow channels: the majority of cells aligned with the flow of growth medium through the device. We reasoned that stronger and sharper autocorrelation signatures should be achieved after employing our new (to our knowledge) cell-alignment protocol. Indeed, autocorrelation analysis of aligned cells produced clear autocorrelation functions, with a single broad peak for nucleoid-associated DnaX-YPet and strong cross peaks for membrane-bound LacY-eYFP at ~0.7 μm from the central peak (Fig. 3, *E* and *F*). We found that, in general, our new (to our knowledge) form of analysis, in which cells were mathematically aligned, was less sensitive to negative effects caused by noncellular background signals than in our earlier flow-aligned approach.

Analysis of spatiotemporal changes in protein localization

Using a combination of time-lapse imaging and autocorrelation analysis of flow-aligned cells, we recently showed that DNA polymerase V (pol V) is subject to spatial regulation as part of the DNA damage response in *E. coli* (20). Cells irradiated with UV light increase production of pol V (Fig. 4, *A* and *B*). The newly synthesized pol V is initially sequestered at the cell membrane, then released into the cytosol during later stages of the DNA damage response, where it acts to bypass UV-induced lesions on the DNA (Fig. 4 *A*). We next determined whether our computational cell-alignment technique could be used to even more clearly visualize these changes in cellular localization. We averaged information from all fields of view at a particular time point, and plotted line scans and autocorrelation functions as functions of time on a two-dimensional (2D) contour plot (Fig. 4, *C*

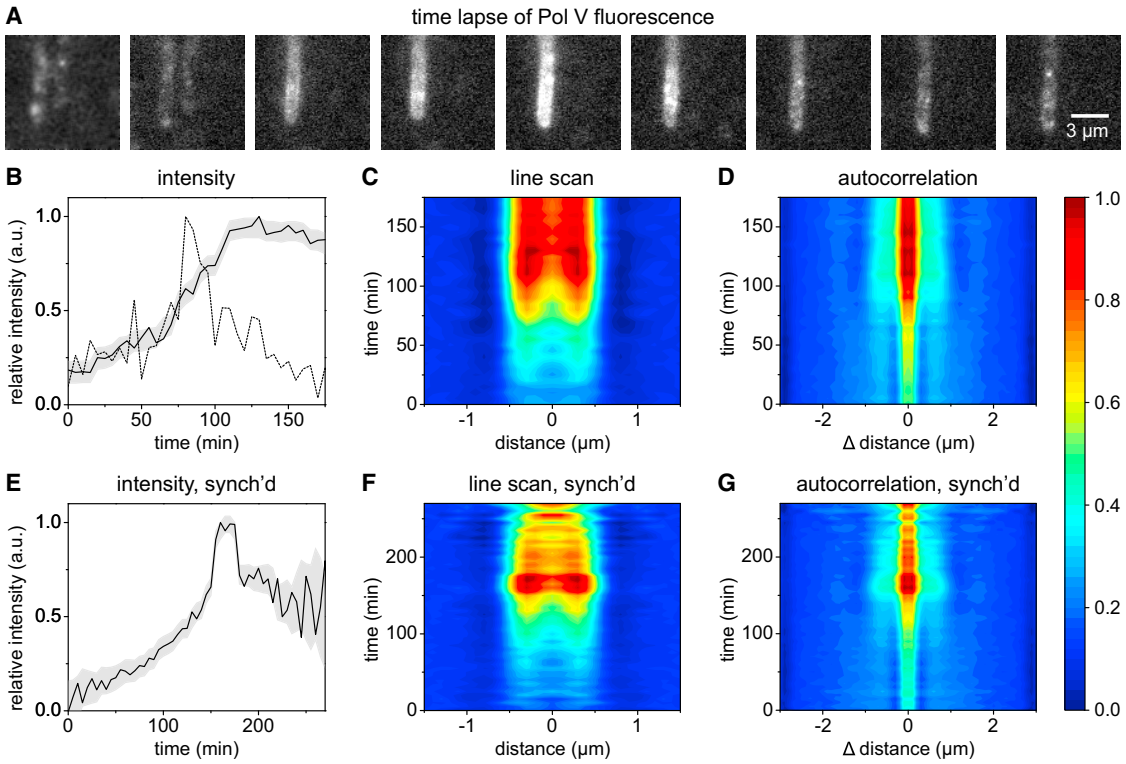

FIGURE 4 Analysis of time-lapse series. (*A*) Time-lapse imaging of fluorescent DNA polymerase V (pol V) shows increased levels in response to DNA damage caused by UV irradiation. The images are acquired at a 10-min interval starting at 40 min after UV radiation. (*B*) The total fluorescence intensity of a single cell (*A*) shows a small peak (*dashed line*), whereas the total intensity of the entire population is severely broadened (*solid line*) because pol V production is not synchronized. (*Shaded area*) Standard error. (*C* and *D*) Average line scan and autocorrelation as a function of time displayed on a 2D contour plot. Redistribution of the protein from being membrane-associated (60–90 min) to cytosolic (90–175 min) can be observed. (*E*) Total intensity after postsynchronization. (*Shaded area*) Standard error. (*F* and *G*) 2D plots from the line scan and autocorrelation approaches after postsynchronization show strong membrane-associated signatures at the peak of pol V levels around 175 min. These signatures later decrease and become cytosolic. To see this figure in color, go online.

and *D*). Both the averaged line-scan approach (Fig. 4 *C*) and the autocorrelation approach (Fig. 4 *D*) show clear evidence of redistribution: membrane-associated signatures are observed in the period 60–90 min after UV irradiation (0 min) and become progressively weaker between 90–175 min.

In our earlier work, we found that changes in the cellular localization of pol V correlate with changes in its concentration (20). The protein is predominantly membrane-associated while its levels increase and gradually redistribute after production ceases. However, the response of individual cells to DNA damage is not synchronized: each cell produces pol V at a different time after UV irradiation (Fig. 4 *B*). We reanalyzed our time-lapse movies with our cell alignment tool using postacquisition synchronization of the signals to the point of maximum intensity (Fig. 4 *E*). This point corresponds to 175 min on our plots. At early (<50 min) and late (>220 min) time-points, the uncertainty is increased as progressively fewer tiles contribute to the average (*shaded area*, Fig. 4 *E*). Plots produced using both the line scan and autocorrelation approaches show strong membrane-associated signatures at the peak of pol V production (175 min), which subsequently decrease and give way to cytosolic signatures (Fig. 4, *F* and *G*).

Quantification of signals within cytosolic and membrane regions of cells

Line scans are direct projections of the nondiffusive protein levels inside the cell and they allow us to quantify relative amounts of protein present in the cytosol or bound to membrane. These average cross sections represent mixtures of purely cytosolic and purely membrane-localized fluorescence signals. Fitting the data to a linear combination of both signals yields the relative contribution of each type of fluorescence. Although the point spread function causes overlap of the both fluorescence types, the shapes of the curves are clearly distinguishable and the combined signal can be reliably decomposed by curve-fitting. To demonstrate this approach, we fit line scans of post-acquisition-synchronized pol V fluorescence with model profiles from data of known cytosolic and membrane-bound proteins (DnaX and LacY (Figs. 3, *C* and *D*, and 5 *A*). In Fig. 5 *B*, the fraction of cytosolic fluorescence is plotted versus time. By multiplying this curve with the total fluorescence (Fig. 4 *E*), we can directly deconstruct this signal into cytosolic (Fig. 5 *C*) and membrane-associated components (Fig. 5 *D*) and thus quantify spatiotemporal changes. These plots show clearly peaked membrane-associated features at 175 min (Fig. 5 *D*). Our analysis indicates that ~90% of pol V signal is associated with the membrane at the peak. Later time points show a clear rise in cytosolic features (Fig. 5 *C*), in direct agreement with prior analyses (Fig. 4, *F* and *G* (20)).

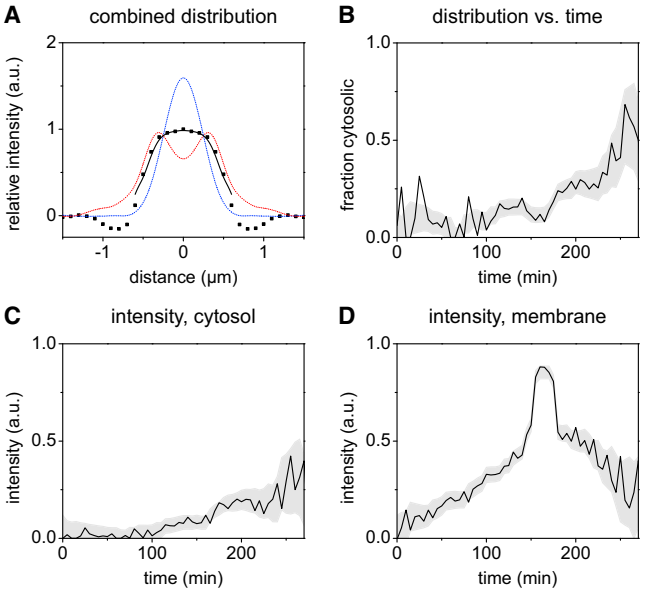

FIGURE 5 Extracting proportions of cytosolic and membrane-associated fluorescence signals from images. (*A*) Line scans are linear combinations of a purely cytosolic and a purely membrane-localized fluorescence signal (*dashed lines*, *blue* and *red*, respectively). The fit (*solid black line*) closely resembles the measured profile (*solid squares*). The curve is fitted in the range from −0.6 to +0.6 μm so that local minima outside this range, which are artifacts of the preprocessing filter (see Image Preparation), are ignored. (*B*) The fraction of cytosolic fluorescence versus time; the shaded area indicates the uncertainty. (*C* and *D*) Based on the previous curve, the total fluorescence intensity (Fig. 4 *E*) can be split into cytosolic and membrane-localized parts. To see this figure in color, go online.

DISCUSSION

Our technique represents, to our knowledge, a novel approach to the analysis of fluorescent protein localization within bacterial cells. The method is fast and requires no manual intervention by the user. A dataset of 444 images runs in ~5 min on a standard desktop computer. The rotational and translational alignment is fairly robust as it is selective against artifacts or cells that are perpendicularly touching each other in one tile (see *fourth tile* in Fig. 2, *C* and *F*). While our tool was developed for analysis of fluorescent protein signals within rod-shaped bacterial cells, it could in principle be used to analyze any type of image containing rod-shaped objects of homogenous width, such as filamentous virus particles and polymer fibers. We envisage that our tool may be particularly useful for analyzing low-contrast images, such as those produced using transmission electron microscopy.

In this article, we demonstrate the use of our tool for analysis of protein localization using data from a single fluorescence color channel. However, we have also developed the capability to carry out two-color colocalization analysis using cross correlation. Such a two-color approach can be used to determine whether patchy features coinhabit the same subcellular regions.

An outstanding and much more difficult problem is to analyze the distributions of proteins along the long axis of bacterial cells. This capability would be particularly useful for analysis of cell-division proteins, such as FtsZ, which tend to accumulate at the midplane of the cell, or for proteins that accumulate at the cell poles, such as the Min proteins (25). For objects of reasonably uniform length, such as log-phase *E. coli* cells (3–6 μm in length), we anticipate that long-axis analysis should be possible; however, robust detection of the cell poles and septum is a significant challenge. We are currently exploring this possibility and foresee that such long-axis analysis may be included in later versions of our tool.

SUPPORTING MATERIAL

Supporting Materials and Methods, three figures, and a zip file containing the codes used in the study are available at http://www.biophysj.org/biophysj/supplemental/S0006-3495(16)30066-2.

AUTHOR CONTRIBUTIONS

J.M.G.H. designed and performed research; contributed analytic tools and analyzed data. A.M.v.O. designed research and A.R. designed and performed research and analyzed data.

ACKNOWLEDGMENTS

A.M.v.O. acknowledges funding from the European Research Council (ERC Starting Grant No. 281098) and the Australian Research Council (grant No. FL140100027).

REFERENCES

1. Yao, Z., and R. Carballido-López. 2014. Fluorescence imaging for bacterial cell biology: from localization to dynamics, from ensembles to single molecules. *Annu. Rev. Microbiol.* 68:459–476.
2. Neidhardt, F. C., J. L. Ingraham, and M. Schaechter. 1990. Physiology of the Bacterial Cell: a Molecular Approach. Sinauer Associates, Sunderland, MA.
3. Bi, E. F., and J. Lutkenhaus. 1991. FtsZ ring structure associated with division in *Escherichia coli*. *Nature.* 354:161–164.
4. Meier, E. L., and E. D. Goley. 2014. Form and function of the bacterial cytokinetic ring. *Curr. Opin. Cell Biol.* 26:19–27.
5. Sliusarenko, O., J. Heinritz, …, C. Jacobs-Wagner. 2011. High-throughput, subpixel precision analysis of bacterial morphogenesis and intracellular spatio-temporal dynamics. *Mol. Microbiol.* 80:612–627.
6. Kamentsky, L., T. R. Jones, …, A. E. Carpenter. 2011. Improved structure, function and compatibility for CellProfiler: modular high-throughput image analysis software. *Bioinformatics.* 27:1179–1180.
7. Jones, T. R., I. H. Kang, …, A. E. Carpenter. 2008. CellProfiler Analyst: data exploration and analysis software for complex image-based screens. *BMC Bioinformatics.* 9:482.
8. Young, J. W., J. C. Locke, …, M. B. Elowitz. 2011. Measuring single-cell gene expression dynamics in bacteria using fluorescence time-lapse microscopy. *Nat. Protoc.* 7:80–88.
9. Guberman, J. M., A. Fay, …, Z. Gitai. 2008. PSICIC: noise and asymmetry in bacterial division revealed by computational image analysis at sub-pixel resolution. *PLOS Comput. Biol.* 4:e1000233.
10. Mekterović, I., D. Mekterović, and Z. Maglica. 2014. BactImAS: a platform for processing and analysis of bacterial time-lapse microscopy movies. *BMC Bioinformatics.* 15:251.
11. Paintdakhi, A., B. Parry, …, C. Jacobs-Wagner. 2015. Oufti: an integrated software package for high-accuracy, high-throughput quantitative microscopy analysis. *Mol. Microbiol.* 99:767–777.
12. van Teeffelen, S., J. W. Shaevitz, and Z. Gitai. 2012. Image analysis in fluorescence microscopy: bacterial dynamics as a case study. *BioEssays.* 34:427–436.
13. Werner, J. N., E. Y. Chen, …, Z. Gitai. 2009. Quantitative genome-scale analysis of protein localization in an asymmetric bacterium. *Proc. Natl. Acad. Sci. USA.* 106:7858–7863.
14. Wolf, L., O. K. Silander, and E. van Nimwegen. 2015. Expression noise facilitates the evolution of gene regulation. *eLife.* 4:4. http://dx.doi.org/10.7554/eLife.05856.
15. Kuwada, N. J., B. Traxler, and P. A. Wiggins. 2015. Genome-scale quantitative characterization of bacterial protein localization dynamics throughout the cell cycle. *Mol. Microbiol.* 95:64–79.
16. Yao, Z., D. Kahne, and R. Kishony. 2012. Distinct single-cell morphological dynamics under β-lactam antibiotics. *Mol. Cell.* 48:705–712.
17. Desmarais, S. M., C. Tropini, …, K. C. Huang. 2015. High-throughput, highly sensitive analyses of bacterial morphogenesis using ultra performance liquid chromatography. *J. Biol. Chem.* 290:31090–31100.
18. van Gestel, J., H. Vlamakis, and R. Kolter. 2015. New tools for comparing microscopy images: quantitative analysis of cell types in *Bacillus subtilis*. *J. Bacteriol.* 197:699–709.
19. Schneider, C. A., W. S. Rasband, and K. W. Eliceiri. 2012. NIH image to ImageJ: 25 years of image analysis. *Nat. Methods.* 9:671–675.
20. Robinson, A., J. P. McDonald, …, A. M. van Oijen. 2015. Regulation of mutagenic DNA polymerase V activation in space and time. *PLoS Genet.* 11:e1005482.
21. Bigün, J., and G. H. Granlund. 1987. Optimal orientation detection of linear symmetry. *In* Proceedings of the IEEE First International Conference on Computer Vision. Institute of Electrical and Electronics Engineers, London, UK, pp. 433–438.
22. Harris, C., and M. Stephens. 1988. A combined corner and edge detector. *In* Proceedings of the 4th Alvey Vision Conference. http://www.bmva.org/bmvc/1988/avc-88-023.pdf. Plessey Research Roke Manor, Romsey, UK. 147–151.
23. Jähne, B. 1993. Spatio-temporal image processing—theory and scientific applications. *In* Lecture Notes in Computer Science, *Vol. 751*. Springer, Berlin, Germany.
24. Reyes-Lamothe, R., D. J. Sherratt, and M. C. Leake. 2010. Stoichiometry and architecture of active DNA replication machinery in *Escherichia coli*. *Science.* 328:498–501.
25. Rowlett, V. W., and W. Margolin. 2013. The bacterial Min system. *Curr. Biol.* 23:R553–R556.